

## Research Papers

# Effect of annealing atmosphere on the phase composition and electrochemical properties of iron-oxide-based electrospun nanofibers

Bo Zhang<sup>a</sup>, Fei Xie<sup>a</sup>, Shujin Hao<sup>a</sup>, Meng Sun<sup>a</sup>, Feiyu Diao<sup>b,\*</sup>, Rongsheng Cai<sup>c,\*</sup>,  
Yiqian Wang<sup>a,\*</sup>

<sup>a</sup> College of Physics, Qingdao University, No. 308 Ningxia Road, Qingdao 266071, PR China

<sup>b</sup> Industrial Research Institute of Nonwovens & Technical Textiles, Shandong Center for Engineered Nonwovens, College of Textile and Clothing, Qingdao University, No. 308 Ningxia Road, Qingdao 266071, PR China

<sup>c</sup> State Key Laboratory of Solid Lubrication, Lanzhou Institute of Chemical Physics, Chinese Academy of Sciences, Lanzhou 730000, PR China

## ARTICLE INFO

## Keywords:

Metal oxide  
Electrospinning  
Annealing atmosphere  
Lithium-ion batteries  
Electrochemical performance

## ABSTRACT

Iron oxide fiber membranes, fabricated by electrospinning and subsequent high-temperature annealing, have promising applications in the binder-free anodes for lithium-ion battery. However, the effect of the annealing atmosphere on the phases of iron oxide fibers and their electrochemical properties has not been elucidated. In this work, iron acetylacetonate/polyacrylonitrile fiber membranes are prepared by electrospinning technique followed by annealing in different atmospheres (argon and air) at 600 °C, and their phases and electrochemical performance are explored. It is found that the membrane annealed in argon is composed of carbon fibers embedded with Fe<sub>3</sub>O<sub>4</sub> nanoparticles, whereas the membrane annealed in air consists primarily of Fe<sub>2</sub>O<sub>3</sub> nanoparticles. When annealed in air, iron keeps its original valence state, and reacts with oxygen, forming Fe<sub>2</sub>O<sub>3</sub>; when annealed in argon, part of iron changes from Fe<sup>3+</sup> to Fe<sup>2+</sup> due to the reduction of carbon, resulting in formation of Fe<sub>3</sub>O<sub>4</sub>. Apart from the phase change, the electrochemical properties show drastic change for the fiber membranes annealed in different atmospheres. The membranes annealed in argon show better cyclic stability than those annealed in air due to the buffering effect of carbon in the fibers. Our work provides insights into the influence of annealing atmosphere on the phase and electrochemical performance of iron-oxide fiber membranes, which is helpful to fabricate binder-free anodes for lithium-ion battery.

## 1. Introduction

Transition metal oxides have emerged as significant candidates for anode materials owing to their distinct advantages such as environmental sustainability, cost-effectiveness, and exceptional electrochemical properties. Among the transition metal oxides, iron oxides, such as Fe<sub>3</sub>O<sub>4</sub> and Fe<sub>2</sub>O<sub>3</sub>, have attracted extensive research attention due to their remarkable theoretical specific capacity and outstanding catalytic activity [1,2].

Recently, researchers have conducted extensive and in-depth research to further improve electrochemical properties of iron oxides. Among various fabrication techniques, electrospinning stands out because it enables mass production of iron oxide fiber membranes that can be utilized as binder-free anodes for lithium-ion batteries [3–5]. The binder-free electrode has advantages of increasing energy density, improving electrochemical performance, and protecting the

environment. Through electrospinning, researchers have successfully fabricated various iron oxide-based fibers, such as carbon-coated Fe<sub>3</sub>O<sub>4</sub> nanofibers and porous Fe<sub>3</sub>O<sub>4</sub> nanofibers [6]. These iron oxide fiber membranes exhibit significant advantages in electrochemical applications, particularly in mitigating volume expansion during charge and discharge cycles, which leads to notable enhancements in electrochemical performance [7]. However, focusing on the performance of electrospun products has raised concerns that the influence of processing conditions on material properties may be underappreciated.

The electrospinning process for fabricating iron oxide fiber membranes consists of two primary stages: electrospinning and annealing [8–11]. In our previous work, we found that the phase composition of iron oxides changes with the annealing temperature [12]. Although the influence of annealing temperature on the phase composition has been explored to some extent, a comprehensive investigation of other processing conditions such as annealing atmosphere remains insufficient.

\* Corresponding authors.

E-mail addresses: [fydiao@qdu.edu.cn](mailto:fydiao@qdu.edu.cn) (F. Diao), [rongshengcai@licp.cas.cn](mailto:rongshengcai@licp.cas.cn) (R. Cai), [yqwang@qdu.edu.cn](mailto:yqwang@qdu.edu.cn) (Y. Wang).

<https://doi.org/10.1016/j.est.2025.116851>

Received 26 January 2025; Received in revised form 11 April 2025; Accepted 27 April 2025

Available online 2 May 2025

2352-152X/© 2025 Elsevier Ltd. All rights are reserved, including those for text and data mining, AI training, and similar technologies.

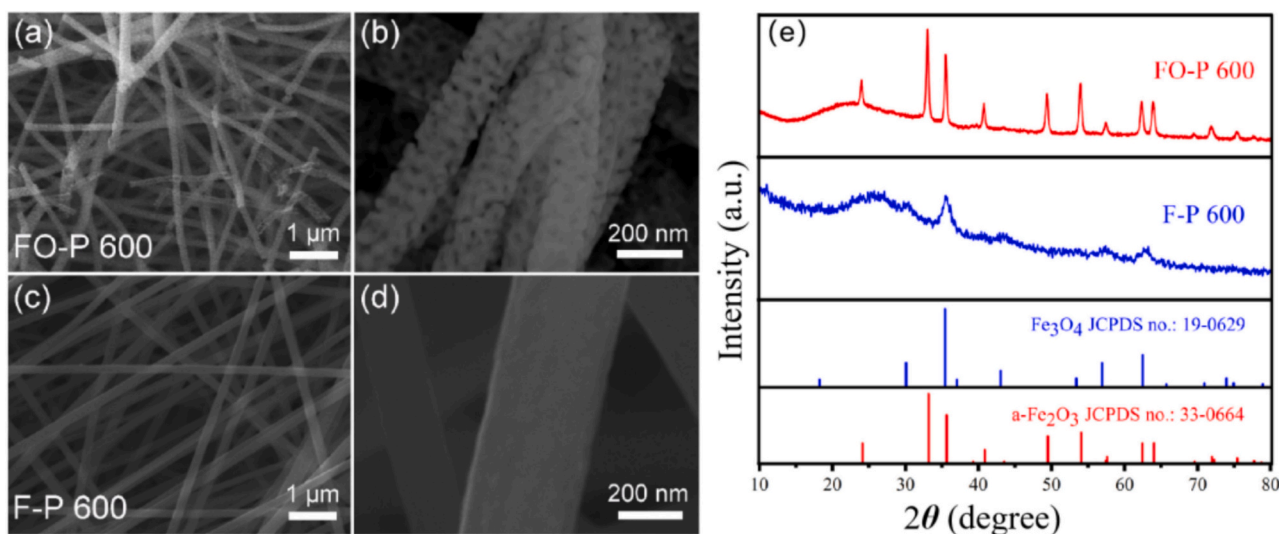


Fig. 1. FE-SEM images of FO-P 600 (a, b) and F-P 600 (c, d), (e) XRD patterns of the FO-P 600 and F-P 600.

Specifically, the effect of annealing atmosphere on composition, morphology, microstructure and electrochemical performance of the electrospun products is an important and under-explored subject that warrants further investigation.

In this work, we investigated the composition and electrochemical properties of iron oxide fiber membrane produced under different annealing atmospheres. The fibers annealed in argon resulted in a carbon matrix embedded with  $\text{Fe}_3\text{O}_4$  nanoparticles, whereas those annealed in air comprised  $\text{Fe}_2\text{O}_3$  nanoparticles. The membranes annealed in argon show better cyclic stability than those annealed in air.

## 2. Experimental section

### 2.1. Materials

Polyacrylonitrile (PAN, average Mw. 150,000), Iron acetylacetonate [ $\text{Fe}(\text{acac})_3$ , 98 %] and *N,N*-Dimethylformamide (DMF, 99.5 %) were purchased from Sinopharm Chemical Reagent Company Limited. All chemicals were of analytical grade and used as received without further purification.

### 2.2. Preparation of iron-based fiber membranes

First, a precursor solution containing DMF, PAN (11 wt%) and  $\text{Fe}(\text{acac})_3$  was prepared, and stirred at 30 °C for 6 h to form a viscous mixture. Then, the fiber membranes were obtained by electrospinning under a working voltage of 16 kV with a flow rate of 0.36 mL/h. The distance between needle tip and collecting roll was set to 16 cm. The receiver speed and needle diameter were 500 rpm and 0.55 mm, respectively. The temperature and the humidity were maintained at 26 °C and 33–36 % during the process. Previous studies [12] indicated that a relatively pure phase could be achieved at 600 °C, so this temperature was selected for the annealing in this work. Finally, the fiber membranes were annealed at 600 °C for 6 h with a heating rate of 2 °C/min in argon or air. The resultant products obtained in argon and air were labeled as F-P 600 and FO-P 600, respectively.

### 2.3. Materials characterization

The crystal structures of as-prepared fiber membranes were investigated using an X-ray diffractometer (XRD, Rigaku) with  $\text{Cu-K}\alpha$  radiation ( $\lambda = 1.5406 \text{ \AA}$ ). Their morphologies were studied using a field-emission scanning electron microscope (FE-SEM, Sigma 500) at an accelerating

voltage of 20 kV. The compositions were determined using an energy dispersive X-ray spectrometer (EDS, Oxford INCAx Sight6427). Bright-field (BF), selected area electron diffraction (SAED) and high-resolution transmission electron microscopy (HRTEM) images were obtained using high-resolution transmission electron microscope (TEM, JSM-2100Plus). High-angle annular dark field (HAADF) images were acquired on scanning transmission electron microscope (STEM, Thermo Scientific Spectra 300).

### 2.4. Electrochemical measurements

Electrochemical test was conducted using a CR2025 coin cell (20 mm in diameter and 2.5 mm in thickness), with lithium metal serving as a counter electrode at ambient temperature. The anodes were prepared by mixing the as-prepared products (FO-P 600 and F-P 600), carbon black and polyvinylidene fluoride (PVDF) in *N*-methylpyrrolidone with a weight ratio of 7:2:1. This mixture was uniformly coated onto copper foil and subsequently dried under vacuum at 120 °C for 12 h. The assembly process was performed in a glove box filled with high-purity argon, ensuring that the concentrations of moisture and oxygen maintained below 0.1 ppm. An electrolyte consisting of a 1 M  $\text{LiPF}_6$  solution mixed with ethylene carbonate (EC), dimethyl carbonate (DMC), and diethyl carbonate (DEC) in a volumetric ratio of 1:1:1 was employed. Rate performance and cycling stability were evaluated using a LAND CT2001 battery test system, operating in a voltage range of 0.01–3.00 V. Cyclic voltammetry (CV) and electrochemical impedance spectroscopy (EIS) tests were carried out on a Metrohm Autolab electrochemical workstation (PGSTAT 302 N). CV curves were obtained at a scan rate of 0.3  $\text{mV s}^{-1}$  over a potential range of 0.01–3.00 V. EIS spectra were recorded at a disturbance amplitude of 5 mV with a frequency range from 100 kHz to 0.01 Hz.

## 3. Results and discussion

To investigate the morphologies of fiber membranes obtained under different annealing atmospheres, FO-P 600 and F-P 600 were examined using SEM. Fig. 1 (a) presents a low-magnification FE-SEM image of FO-P 600, revealing a fibrous morphology. In Fig. 1 (b), a high-magnification FE-SEM image further illustrates that the surface of the fibers exhibits numerous pores. The average diameter of the fibers is approximately 150 nm. Fig. 1 (c) and (d) display low and high magnification FE-SEM images of F-P 600, respectively. These images indicate that F-P 600 exhibits a fibrous structure signified by uniform dimensions and a

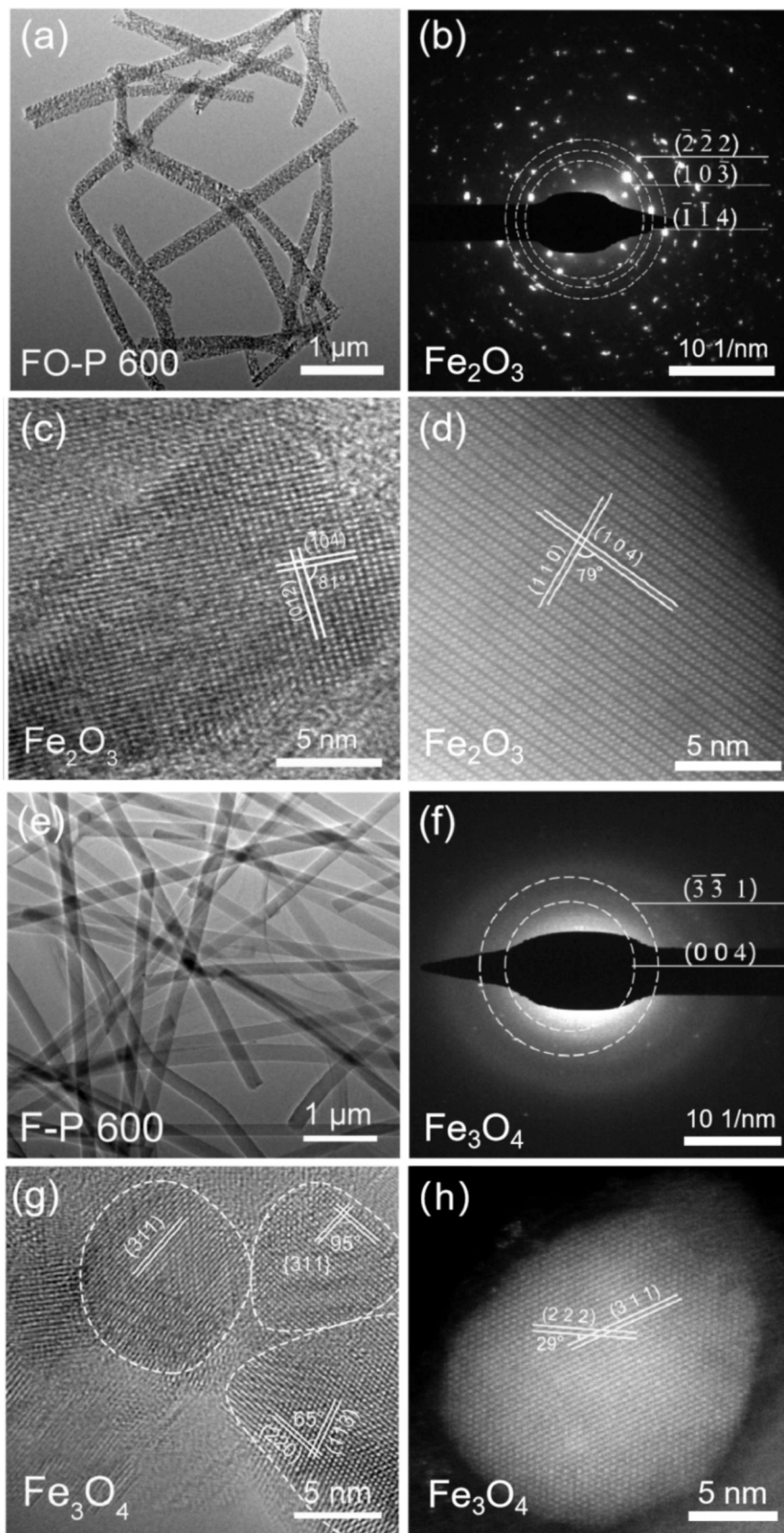


Fig. 2. Typical BF TEM, corresponding SAED pattern, HRTEM and HAADF images of FO-P 600 (a, b, c and d) and F-P 600 (e, f, g and h).

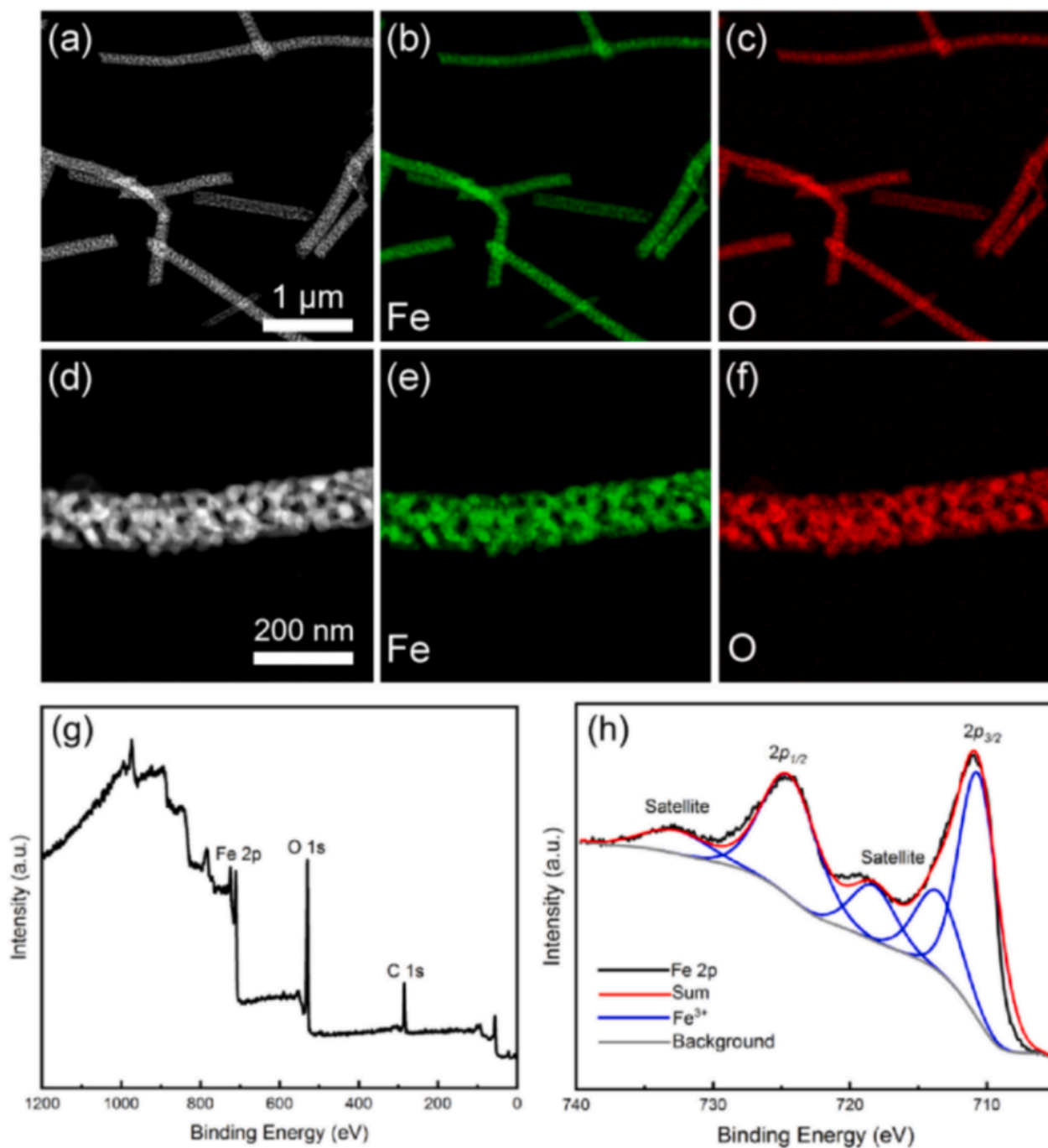


Fig. 3. STEM images (a, d) and EDS elemental mappings (b, c, e and f) of FO-P 600; Full-scan XPS spectra (g) and high-resolution spectra (h) of Fe 2p in FO-P 600.

smooth surface, with an average fiber diameter of approximately 190 nm. In addition, we conducted BET (Brunauer-Emmett-Teller) test on F-P 600 and FO-P 600 samples. Fig. S1 shows the  $N_2$  adsorption-desorption isotherms of F-P 600 and FO-P 600. It can be seen from Fig. S1 that FO-P 600 has an isotherm characteristic of mesoporous materials, which is consistent with our SEM observation. The BET surface area of F-P 600 and FO-P 600 is measured to be  $9.03 \text{ m}^2 \text{ g}^{-1}$  and  $20.61 \text{ m}^2 \text{ g}^{-1}$ , respectively. Fig. 1(e) depicts the XRD patterns for FO-P 600 and F-P 600. For FO-P 600, the diffraction peaks belong to the rhombohedral phase of  $\text{Fe}_2\text{O}_3$  (JCPDS no.: 33-0664,  $a = b = 5.0356 \text{ \AA}$ ,  $c = 13.7489 \text{ \AA}$ ,  $\alpha = \beta = 90^\circ$ ,  $\gamma = 120^\circ$ ) [13]. For F-P 600, the peak observed at  $26^\circ$  is attributed to amorphous carbon, while the other diffraction peaks at  $30.1^\circ$ ,  $35.4^\circ$ ,  $43.1^\circ$ ,  $56.9^\circ$  and  $62.5^\circ$  correspond to (220), (311), (400), (511) and (440) planes of cubic  $\text{Fe}_3\text{O}_4$  (JCPDS no.: 19-0629,  $a = 8.396$

$\text{\AA}$ ) [14]. The XRD analysis indicates that FO-P 600 is composed of  $\text{Fe}_2\text{O}_3$ , whereas F-P 600 consists of carbon and  $\text{Fe}_3\text{O}_4$ .

To further elucidate the microstructure of FO-P 600 and F-P 600, comprehensive TEM investigations were carried out. Fig. 2(a) displays a low-magnification BF TEM image of FO-P 600 revealing an average fiber diameter of approximately 150 nm, and Fig. 2(b) illustrates the corresponding diffraction pattern [15]. The observed diffraction rings from the innermost to outermost are attributed to the (10 $\bar{3}$ ), (1 $\bar{1}$ 4), (2 $\bar{2}$ 2) planes of rhombohedral  $\text{Fe}_2\text{O}_3$ , which agrees well with the XRD analysis. A typical HRTEM image of nanoparticles in the FO-P 600 is presented in Fig. 2(c). The measured lattice spacings are 3.71  $\text{\AA}$  and 2.70  $\text{\AA}$ , corresponding to the (012) and ( $\bar{1}$ 04) crystal planes of rhombohedral  $\text{Fe}_2\text{O}_3$ , respectively. The angle between the crystal planes is  $81^\circ$ , aligning with

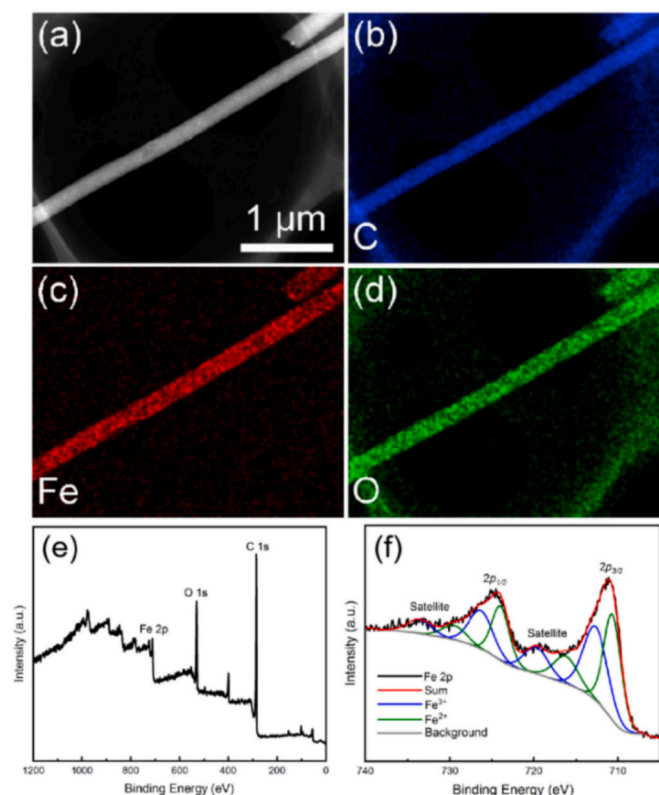


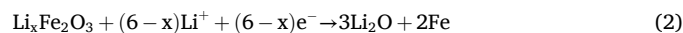
Fig. 4. STEM images (a) and EDS elemental mappings (b, c and d) of F-P 600; Full-scan XPS spectra (e) and high-resolution spectra (f) of Fe 2p in the F-P 600.

the theoretical prediction. In Fig. 2(d), the lattice spacings are measured to be 2.52 Å and 2.70 Å, corresponding to the (110) and ( $\bar{1}04$ ) crystal planes of rhombohedral phase  $\text{Fe}_2\text{O}_3$ , with the angle of 79°. The XRD and FE-SEM analyses confirm that FO-P 600 is composed of  $\text{Fe}_2\text{O}_3$  nanoparticles embedded within a fibrous matrix. Fig. 2(e) shows a low-magnification BF TEM image of F-P 600, demonstrating a uniform fiber diameter distribution with an average fiber diameter of approximately 190 nm. Fig. 2(f) illustrates the diffraction pattern of Fig. 2(e), in which the diffraction rings from the innermost to outermost correspond to the (004) and ( $3\bar{3}1$ ) planes of cubic  $\text{Fe}_3\text{O}_4$ . The polycrystalline rings exhibit limited visibility, indicating the poor crystallinity of F-P 600, which is attributed to the carbon content within the fiber and the small size of the  $\text{Fe}_3\text{O}_4$  particles (less than 10 nm). The HRTEM image in Fig. 2(g) confirms that the nanoparticles in the F-P 600 are  $\text{Fe}_3\text{O}_4$ , which is further corroborated by the HAADF image in Fig. 2(h). The distinct compositions of FO-P 600 and F-P 600 underscore the significant impact of the annealing atmosphere on the resultant products.

The elemental distributions and the valence state of Fe in FO-P 600 and F-P 600 are explored by EDS and XPS, respectively. Figs. 3(a) and (d) present STEM images of FO-P 600 at different magnifications, confirming that the product is fibers composed of nanoparticles. Figs. 3(b-f) illustrate the elemental distribution of Fe and O within the fibers. A comparative analysis of the EDS elemental mappings indicates that the nanoparticles are primarily composed of Fe and O. Combined with XRD and TEM results, it is confirmed that the FO-P 600 is composed of  $\text{Fe}_2\text{O}_3$  nanoparticles. To assess the valence state of Fe in the FO-P 600, XPS was carried out. Fig. 3(g) displays a full-scan XPS spectrum for the FO-P 600, and Fig. 3(h) specifically shows the high-resolution spectrum of the Fe 2p. The peaks at 711 eV and 724 eV correspond to the Fe  $2p_{3/2}$  and Fe  $2p_{1/2}$  states, respectively [16,17]. The peaks at 714 eV, 718 eV and 733 eV represent satellite peaks associated with  $\text{Fe}^{3+}$  [18,19]. This indicates that the valence state of Fe in the FO-P 600 is trivalent, confirming that the FO-P 600 is composed of  $\text{Fe}_2\text{O}_3$ . Fig. 4(a) presents a low-

magnification STEM image of F-P 600, and Figs. 4(b-d) illustrate the elemental distribution images of C, Fe and O within the fiber, respectively. It can be concluded that the F-P 600 is composed of three elements: C, Fe and O. This further corroborates that F-P 600 contains carbon fibers loaded with  $\text{Fe}_3\text{O}_4$  nanoparticles. Fig. 4(f) shows a high-resolution spectrum of the Fe 2p in the F-P 600, which reveals two peaks at 711 eV and 724 eV belonging to the Fe  $2p_{3/2}$  and Fe  $2p_{1/2}$  states, respectively. Peak fitting analysis reveals that each of these peaks is further resolved into two sub-peaks. Specifically, the peaks at 710 eV and 724 eV are attributed to  $\text{Fe}^{2+}$ , while the peaks at 712 eV and 726 eV correspond to  $\text{Fe}^{3+}$ . The peaks at 716 eV, 720 eV, 730 eV and 733 eV are satellite peaks of Fe 2p [20]. Fig. S2 shows the high-resolution spectra of the O 1s in F-P 600 and FO-P 600. The peaks at 530 eV and 532 eV correspond to lattice oxygen and surface defect sites, respectively [21]. Through the above analysis, it is evident that both  $\text{Fe}^{2+}$  and  $\text{Fe}^{3+}$  species are present in F-P 600, confirming that it is composed of  $\text{Fe}_3\text{O}_4$  [22].

The anode materials, FO-P 600 and F-P 600, are evaluated for their electrochemical performances. Fig. 5(a) shows the CV curve of the initial six cycles of the FO-P 600 electrode at a scanning rate of 0.3  $\text{mV s}^{-1}$ . The CV profile reveals reduction peaks at 1.2 V, 0.7 V and 0.3 V, along with an oxidation peak at 2.0 V. The reduction peaks at 1.2 V and 0.7 V are associated with structural transformations caused by lithium intercalation and further reduction of  $\text{Li}_x\text{Fe}_2\text{O}_3$  to  $\text{Fe}^0$  via a conversion reaction. The equations for the above electrochemical reaction are displayed as follows [23].



The reduction peak at 0.3 V is indicative of the formation of solid electrolyte interphase (SEI) film [24]. The oxidation peak at 2.0 V corresponds to the delithiation process of the electrode material and the oxidation of  $\text{Fe}^0$  to  $\text{Fe}^{3+}$ . In subsequent cycles, the redox peaks shift to higher potentials, indicating a poor cyclic stability for FO-P 600.

Fig. 5(b) shows the CV curves for the first six cycles of F-P 600 recorded at a scan rate of 0.3  $\text{mV s}^{-1}$ . During the anodic and cathodic processes of the first cycle, two peaks, a reduction peak at 0.6 V and an oxidation peak at 1.2 V, are observed. The reduction peak at 0.6 V corresponds to the formation of  $\text{Fe}^0$ ,  $\text{Li}_2\text{O}$  and SEI film. The equation for the electrochemical reaction is displayed as follows [25].



During the anodic process, the oxidation peak at 1.2 V corresponds to the oxidation of  $\text{Fe}^0$ , represented by the following electrochemical reaction [26].



This process is classified as a transformation reaction. In the following redox process, the reduction peak shifts to 0.7 V due to the irreversibility of the SEI film and electrode polarization. The oxidation peak moves to 1.4 V, and the CV curves exhibit similar peak heights after the second cycle, indicating that the F-P 600 has excellent cycling stability [27,28]. It is evident that the lithium storage mechanism changes significantly for the products obtained in different annealing atmospheres. Specifically, the lithium storage of the F-P 600 electrode predominantly occurs through a conversion reaction, while the lithium storage behavior of FO-P 600 is mainly governed by a pseudocapacitive process. The above SEM and TEM observations reveal a substantial presence of voids in FO-P 600, which provides numerous channels conducive to lithium intercalation.

Fig. 5(c) illustrates the cycling performance of the FO-P 600 and F-P 600 electrodes at a current density of 0.2  $\text{A g}^{-1}$ . In the first ten cycles, the specific capacity of FO-P 600 exceeds that of F-P 600, as the theoretical specific capacity of  $\text{Fe}_2\text{O}_3$  (1007  $\text{mAh g}^{-1}$ ) is higher than that of carbon (372  $\text{mAh g}^{-1}$ ) and  $\text{Fe}_3\text{O}_4$  (926  $\text{mAh g}^{-1}$ ). Furthermore, larger specific

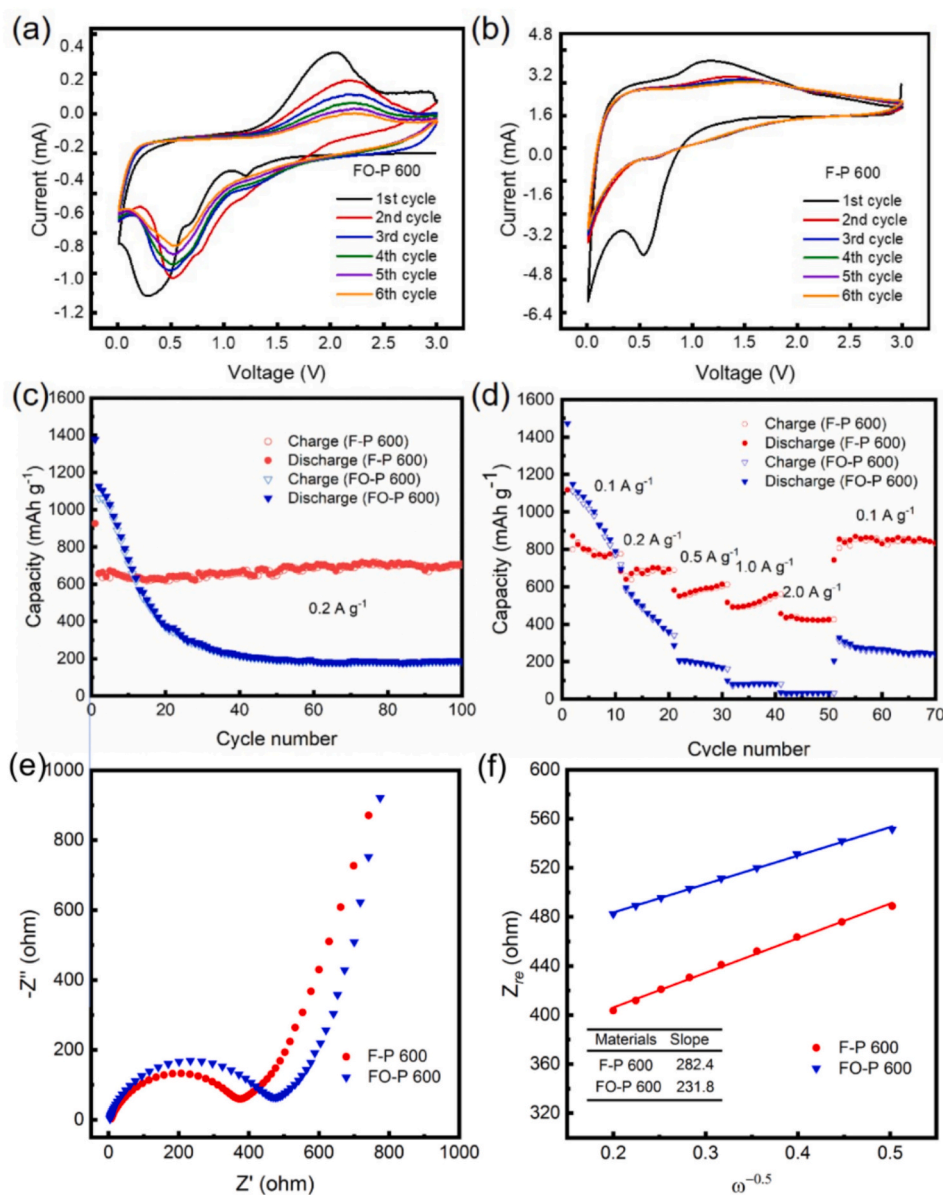


**Fig. 5.** Electrochemical performance of FO-P 600 and F-P 600. CV curves of FO-P 600 (a) and F-P 600 (b) at a scanning rate of 0.3 mV s<sup>-1</sup>, (c) Cycling performance at 0.2 A g<sup>-1</sup>, (d) Rate performance at various current densities, (e) EIS spectra and (f) Graph of  $Z_{re}$  plotted against  $\omega^{-0.5}$  for FO-P 600 and F-P 600.

surface area of FO-P 600 plays a crucial role in its higher specific capacity. After 100 cycles, the specific discharge capacities of F-P 600 and FO-P 600 electrodes are 709.0 and 187.2 mAh g<sup>-1</sup>, respectively. The specific capacity of the F-P 600 electrode exhibits an initial decrease followed by an increase during the charging and discharging processes due to the occurrence of irreversible reactions and the gradual activation of the electrode material upon increasing cycles [30]. The superior cycling stability of the F-P 600 is attributed to the incorporation of carbon, which mitigates the volume expansion of nanoparticles during the charge and discharge processes, thereby enhancing their cycling stability.

In addition, we carried out the cyclic performance of F-P 600 and FO-P 600 electrodes under large current (1 A g<sup>-1</sup>) [29]. In Fig. S3, after 100 cycles under 1 A g<sup>-1</sup>, the specific discharge capacities of F-P 600 and FO-P 600 electrodes are 473.6 and 87.2 mAh g<sup>-1</sup>, respectively. The superior cycling stability of the F-P 600 is attributed to the incorporation of carbon, which mitigates the volume expansion of nanoparticles during charge and discharge processes, thereby enhancing their cycling stability [31]. SEM images obtained after 100 cycles, as shown in Fig. S4,

support this conclusion. F-P 600 and FO-P 600 exhibit different behaviors of structural degradation. Compared to FO-P 600, F-P 600 retains a relatively intact fiber structure, which contributes to its superior cycling stability.

Fig. 5(d) demonstrates the rate performance of the FO-P600 and F-P 600 electrodes. The average specific discharge capacities of the F-P 600 electrode at current densities of 0.1 A g<sup>-1</sup>, 0.2 A g<sup>-1</sup>, 0.5 A g<sup>-1</sup>, 1.0 A g<sup>-1</sup> and 2.0 A g<sup>-1</sup> are 827.9 mAh g<sup>-1</sup>, 761.2 mAh g<sup>-1</sup>, 583.7 mAh g<sup>-1</sup>, 518.3 mAh g<sup>-1</sup> and 431.2 mAh g<sup>-1</sup> respectively. Notably, the specific capacity of F-P 600 is lower than that of FO-P 600 at 0.1 A g<sup>-1</sup>. However, at higher current densities, it significantly exceeds that of FO-P 600. When the current density returns to 0.1 A g<sup>-1</sup>, the average specific discharge capacity of F-P 600 maintains at 841.3 mAh g<sup>-1</sup>, indicating that electrode had excellent rate capability [32]. The observed increase in specific discharge capacity is attributed to the enhanced activation of the F-P 600 electrode at a high current density.

EIS spectra are performed to investigate the electrochemical reaction kinetics of FO-P 600 and F-P 600 electrodes, as displayed in Fig. 5(e). The EIS spectra for both electrodes display a characteristic semicircle in

the high-frequency region, indicative of charge transfer resistance, and an inclined line at lower frequencies, which suggests diffusion-controlled processes. These spectra can be fitted using an equivalent circuit, where  $R_s$ ,  $R_{ct}$ ,  $W$  and CPE represent electrolyte resistance, charge transfer resistance, Warburg impedance and double layer capacitance, respectively [33]. Upon fitting the high-frequency region, the  $R_{ct}$  values of the FO-P 600 and F-P 600 electrodes were 395.0 and 312.0  $\Omega$ , respectively, while the  $R_s$  values of the FO-P 600 and F-P 600 electrodes were determined to be 3.8 and 6.6  $\Omega$ , respectively. The lower  $R_{ct}$  values for F-P 600 suggest better electrical conductivity, which enhances charge transport compared to FO-P 600 [34]. In addition, EIS measurements were performed on the FO-P 600 and F-P 600 electrodes after cycling, and the results were presented in Fig. S5. The  $R_{ct}$  of FO-P 600 and F-P 600 increases to 524.4  $\Omega$  and 354.0  $\Omega$ , respectively, while their  $R_s$  changes to 6.2  $\Omega$  and 8.3  $\Omega$ , respectively. The entire impedance spectrum exhibits an obvious rightward shift, indicating an overall increase of the impedance. The slope of the inclined line in the low frequency region of the EIS spectra correlates with the lithium-ion diffusion coefficient ( $D_{Li}$ ) of the electrode. The value of  $D_{Li}$  can be calculated by Eqs. (5) and (6) [35].

$$D_{Li} = \frac{R^2 T^2}{2 A^2 n^4 F^4 C^2 \sigma^2} \quad (5)$$

$$Z = R_s + R_{ct} + \sigma \omega^{-0.5} \quad (6)$$

where the value of the gas constant  $R$  is 8.314  $J k^{-1} mol^{-1}$ , the temperature  $T$  is 298.15 K, the electrode area  $A$  is  $1.54 \times 10^{-4} m^2$ ,  $n$  is the number of electrons per molecule participating in the electron transfer reaction, the Faraday constant  $F$  is 96,485  $C mol^{-1}$ , and  $C$  is the concentration of lithium ions in the battery [36]. Fig. 5(f) shows the fitting diagram of  $Z_{re}$  and  $\omega^{-0.5}$ . The table, inset in Fig. 5(f), summarizes the  $\sigma$  values of the FO-P 600 and F-P 600 electrodes. Based on Equ. (5), the  $D_{Li}$  for FO-P 600 and F-P 600 electrodes is calculated to be  $9.5 \times 10^{-18}$  and  $5.8 \times 10^{-18} cm^2 s^{-1}$ , respectively. These results indicate that the FO-P 600 electrode exhibits a higher lithium-ion diffusion capacity, suggesting that its porous structure facilitates enhanced lithium-ion transport.

#### 4. Conclusions

The iron acetylacetonate/polyacrylonitrile fiber membrane was prepared by electrospinning and subsequent annealing in argon and air at 600 °C. Upon annealing in an argon, the resultant material consisted of carbon fibers embedded with  $Fe_3O_4$  nanoparticles; when annealing in air, the final product was fibers composed of  $Fe_2O_3$  nanoparticles. During the annealing process in argon, the carbon in the precursor material is preserved due to the inert atmosphere, leading to the formation of carbon fibers embedded with  $Fe_3O_4$  nanoparticles. In contrast, the annealing in air leads to the oxidation of the carbon, resulting in fibers predominantly containing  $Fe_2O_3$  nanoparticles. When utilized as anode materials for lithium-ion batteries, the FO-P 600 exhibited a high initial specific capacity, which is attributed to its superior lithium-ion diffusion properties. However, it demonstrated poor cycling stability. Whereas, the F-P 600 electrode shows better cycle stability and enhanced rate performance compared to the FO-P 600 electrode. This discrepancy in performance is ascribed to two primary factors: (1) the  $Fe_2O_3$  nanoparticles in the FO-P 600 electrode undergo significant volume expansion during the charge and discharge cycles, resulting in particle pulverization and agglomeration of the electrode materials; (2) the carbon in F-P 600 electrode mitigates the volume expansion of  $Fe_3O_4$  nanoparticles during cycling, thereby improving the structural integrity and electrochemical performance of the electrode. This work provides insights into the influence of annealing atmosphere on the phase and electrochemical performance of iron-oxide fiber membranes, which is helpful to fabricate binder-free anodes for lithium-ion battery.

#### CRedit authorship contribution statement

**Bo Zhang:** Writing – original draft. **Fei Xie:** Data curation. **Shujin Hao:** Software, Methodology. **Meng Sun:** Data curation. **Feiyu Diao:** Writing – review & editing. **Rongsheng Cai:** Data curation. **Yiqian Wang:** Writing – review & editing.

#### Declaration of competing interest

There are no conflicts to declare.

#### Acknowledgments

The authors gratefully acknowledge the financial support from the High-end Foreign Experts Programs of the Ministry of Science and Technology, China (Grant Nos.: G2022025015L, G2022025016L), and Shandong Province “Double-Hundred Talent Plan” Program (Grant No.: WST2018006). Y. Q. Wang acknowledges the support from the Taishan Scholar Program of Shandong Province, China, the Qingdao International Center of Semiconductor Photoelectric Nanomaterials, and the Shandong Provincial University Key Laboratory of Optoelectrical Material Physics and Devices.

#### Appendix A. Supplementary data

Supplementary data to this article can be found online at <https://doi.org/10.1016/j.est.2025.116851>.

#### Data availability

Data will be made available on request.

#### References

- [1] L. Ji, O. Toprakci, M. Alcoutlabi, Y. Yao, Y. Li, S. Zhang, B. Guo, Z. Lin, X. Zhang,  $\alpha$ - $Fe_2O_3$  nanoparticle-loaded carbon nanofibers as stable and high-capacity anodes for rechargeable lithium-ion batteries, *ACS Appl. Mater. Interfaces* 4 (2012) 2672–2679.
- [2] H. Zhang, M. Zhang, R. Liu, T. He, L. Xiang, X. Wu, Z. Piao, Y. Jia, C. Zhang, H. Li, F. Xu, G. Zhou, Y. Mai, Fe<sub>3</sub>O<sub>4</sub>-doped mesoporous carbon cathode with a plumber's nightmare structure for high-performance Li-S batteries, *Nat. Commun.* 15 (2024) 5451.
- [3] J. Wang, X. Sheng, S. Hao, G. Liu, R. Cai, X. Xue, Y. Wang, Construction of  $Fe_{0.64}Ni_{0.36}$ @graphite nanoparticles via corrosion-like transformation from  $NiFe_2O_4$  and surface graphitization in flexible carbon nanofibers to achieve strong wideband microwave absorption, *J. Colloid Interface Sci.* 657 (2024) 193–207.
- [4] F. Xie, M. Sun, X. Sheng, Q. Zhang, Z. Ling, S. Hao, F. Diao, Y. Wang, Graphene-wrapped  $Fe_2TiO_5$  nanoparticles with enhanced performance as lithium-ion battery anode, *Mater. Lett.* 358 (2024) 135877.
- [5] S. Hao, X. Sheng, F. Xie, M. Sun, F. Diao, Y. Wang, Electrospun carbon nanofibers embedded with heterostructured  $NiFe_2O_4/Fe_{0.64}Ni_{0.36}$  nanoparticles as an anode for high-performance lithium-ion battery, *J. Energy Storage* 80 (2024) 110412.
- [6] R. Shi, C. Han, X. Xu, X. Qin, L. Xu, H. Li, J. Li, C. Wong, B. Li, Electrospun N-doped hierarchical porous carbon nanofiber with improved degree of graphitization for high-performance lithium ion capacitor, *Chem. Eur. J.* 24 (2018) 10460–10467.
- [7] M.E. Im, D. Pham-Cong, J.Y. Kim, H.S. Choi, J.H. Kim, J.P. Kim, J. Kim, S.Y. Jeong, C.R. Cho, Enhanced electrochemical performance of template-free carbon-coated iron (II, III) oxide hollow nanofibers as anode material for lithium-ion batteries, *J. Power Sources* 284 (2015) 392–399.
- [8] D. Li, K. Wang, H. Tao, X. Hu, S. Cheng, K. Jiang, Facile synthesis of an  $Fe_3O_4/FeO/Fe/C$  composite as a high-performance anode for lithium-ion batteries, *RSC Adv.* 6 (2016) 89715–89720.
- [9] S. Ru, X. Wang, G. Ma, J. Tan, H. Xiao, Z. Ai, Phase inversion synthesis of  $Fe_3O_4@NC$  composites with superior lithium storage performance, *J. Alloys Compd.* 844 (2020) 156039.
- [10] X. Qin, H. Zhang, J. Wu, X. Chu, Y. He, C. Han, C. Miao, S. Wang, B. Li, F. Kang,  $Fe_3O_4$  nanoparticles encapsulated in electrospun porous carbon fibers with a compact shell as high-performance anode for lithium ion batteries, *Carbon* 87 (2015) 347–356.
- [11] H. Wang, Y. Zhou, Y. Shen, Y. Li, Q. Zuo, Q. Duan, Fabrication, formation mechanism and the application in lithium-ion battery of porous  $Fe_2O_3$  nanotubes via single-spinneret electrospinning, *Electrochim. Acta* 158 (2015) 105–112.
- [12] X. Sheng, T. Li, M. Sun, G. Liu, Q. Zhang, Z. Ling, S. Gao, F. Diao, J. Zhang, R. Federico, Y. Wang, Flexible electrospun iron compounds/carbon fibers: phase transformation and electrochemical properties, *Electrochim. Acta* 407 (2022) 139892.

- [13] G. Song, M. Wei, J. Zhou, L. Mu, S. Song, Modulation of the phase transformation of Fe<sub>2</sub>O<sub>3</sub> for enhanced water oxidation under a magnetic field, *ACS Catal.* 14 (2024) 846–856.
- [14] F. Chen, X. Chen, P. Li, J. Zhang, W. Li, G. Wang, H. Zhou, Y. Xie, Z. Chen, C. Liu, Biochar/ $\alpha$ -Fe<sub>2</sub>O<sub>3</sub>/ $\gamma$ -Fe<sub>2</sub>O<sub>3</sub> heterojunction composite for photocatalytic removal of amino black, *ChemistrySelect* 4 (2024) 9.
- [15] L. Zhang, P. Li, W. Mi, E. Jiang, H. Bai, Positive and negative magnetoresistance in Fe<sub>3</sub>O<sub>4</sub>-based heterostructures, *J. Magn. Magn. Mater.* 324 (2012) 3731–3736.
- [16] J. Wang, X. Xue, Y. Wang, Tuning the structural and magnetic properties of electrospun strontium-iron-oxide nanofibers with different stoichiometry, *Mater. Charact.* 200 (2023) 112884.
- [17] J. Sun, W. Xia, Q. Zheng, X. Zeng, W. Liu, G. Liu, P. Wang, Increased active sites on irregular morphological  $\alpha$ -Fe<sub>2</sub>O<sub>3</sub> nanorods for enhanced photoelectrochemical performance, *ACS Omega* 5 (2020) 12339–12345.
- [18] C. Liu, S. Yang, L. Ma, Y. Peng, A. Hamidreza, H. Chang, J. Li, Comparison on the performance of  $\alpha$ -Fe<sub>2</sub>O<sub>3</sub> and  $\gamma$ -Fe<sub>2</sub>O<sub>3</sub> for selective catalytic reduction of nitrogen oxides with ammonia, *Catal. Lett.* 143 (2013) 697–704.
- [19] L. Wang, Y. Huang, X. Sun, H. Huang, P. Liu, M. Zong, Y. Wang, Synthesis and microwave absorption enhancement of graphene@Fe<sub>3</sub>O<sub>4</sub>@SiO<sub>2</sub>@NiO nanosheet hierarchical structures, *Nanoscale* 6 (2014) 3157–3164.
- [20] M. Imran, N. Zouli, T. Ahamad, S.M. Alshehri, M.R. Chandan, S. Hussain, A. Aziz, M.A. Dar, A. Khan, Carbon-coated Fe<sub>3</sub>O<sub>4</sub> core-shell super-paramagnetic nanoparticle-based ferrofluid for heat transfer applications, *Nanoscale Adv.* 3 (2021) 1962–1975.
- [21] T. Li, J. He, B. Peña, C.P. Berlinguette, Curing BiVO<sub>4</sub> photoanodes with ultraviolet light enhances photoelectrocatalysis, *Angew. Chem. Int. Ed.* 55 (2016) 1769–1772.
- [22] C. Jin, Y. Qu, M. Wang, J. Han, Y. Hu, R. Guo, Aqueous solution-based Fe<sub>3</sub>O<sub>4</sub> seed-mediated route to hydrophilic Fe<sub>3</sub>O<sub>4</sub>-Au janus nanoparticles, *Langmuir* 32 (2016) 4595–4601.
- [23] T. Li, S. Gao, K. Li, G. Liu, X. Sheng, D. Shang, L. Wu, S. Chen, Y. Wang, S. Wu, Tailoring the phase evolution of molybdenum-based nanocrystals in carbon nanofibers for enhanced performance of lithium-ion batteries, *J. Alloys Compd.* 934 (2023) 168042.
- [24] Y. Shi, B. Guo, S. Corr, Q. Shi, Y. Hu, K. Heier, L. Chen, R. Seshadri, G. Stuck, Ordered mesoporous metallic MoO<sub>2</sub> materials with highly reversible lithium storage capacity, *Nano Lett.* 9 (2009) 4215–4220.
- [25] H. Lyu, J. Liu, S. Qiu, Y. Cao, C. Hu, S. Guo, Z. Guo, Carbon composite spun fibers with *in situ* formed multicomponent nanoparticles for a lithium-ion battery anode with enhanced performance, *J. Mater. Chem. A* 4 (2016) 9881–9889.
- [26] L. Yang, J. Hu, A. Dong, D. Yang, Novel Fe<sub>3</sub>O<sub>4</sub>-CNTs nanocomposite for Li-ion batteries with enhanced electrochemical performance, *Electrochim. Acta* 144 (2014) 235–242.
- [27] Q. Wu, R. Zhao, X. Zhang, W. Li, R. Xu, G. Diao, M. Chen, Synthesis of flexible Fe<sub>3</sub>O<sub>4</sub>/C nanofibers with buffering volume expansion performance and their application in lithium-ion batteries, *J. Power Sources* 359 (2017) 7–16.
- [28] X. Xu, R. Cao, S. Jeong, J. Cho, Spindle-like mesoporous  $\alpha$ -Fe<sub>2</sub>O<sub>3</sub> anode material prepared from MOF template for high-rate lithium batteries, *Nano Lett.* 12 (2012) 4988–4991.
- [29] Q. Zhu, C. Hu, Y. Xu, Y. Jin, J. Shui, Performance improvement of lithium-ion battery by pulse current, *J. Energy Chem.* 46 (2020) 208–214.
- [30] M. Balogun, Z. Wu, Y. Luo, W. Qiu, X. Fan, B. Long, M. Huang, P. Liu, Y. Tong, High power density nitrated hematite ( $\alpha$ -Fe<sub>2</sub>O<sub>3</sub>) nanorods as anode for high-performance flexible lithium ion batteries, *J. Power Sources* 308 (2016) 7–17.
- [31] F. Xie, X. Sheng, Z. Ling, S. Hao, Q. Zhang, M. Sun, G. Liu, F. Diao, Y. Wang, Flexible electrospun iron/manganese-based compounds/carbon fibers: phase transformation and electrochemical properties, *Electrochim. Acta* 470 (2023) 143288.
- [32] Y. Su, H. Jiang, Y. Zhu, X. Yang, J. Shen, W. Zou, J. Chen, C. Li, Enriched graphitic N-doped carbon-supported Fe<sub>3</sub>O<sub>4</sub> nanoparticles as efficient electrocatalysts for oxygen reduction reaction, *J. Mater. Chem. A* 2 (2014) 7281–7287.
- [33] Q. Wu, R. Yu, Z. Zhou, H. Liu, R. Jiang, Encapsulation of a core-shell porous Fe<sub>3</sub>O<sub>4</sub>@carbon material with reduced graphene oxide for Li<sup>+</sup> battery anodes with long cyclability, *Langmuir* 37 (2021) 785–792.
- [34] L. Guo, H. Sun, C. Qin, W. Li, F. Wang, W. Song, J. Du, F. Zhong, Y. Ding, Flexible Fe<sub>3</sub>O<sub>4</sub> nanoparticles/N-doped carbon nanofibers hybrid film as binder-free anode materials for lithium-ion batteries, *Appl. Surf. Sci.* 459 (2018) 263–270.
- [35] J. Wang, H. He, Z. Wu, J. Liang, L. Han, H. Xin, X. Guo, Y. Zhu, D. Wang, Controllable construction of flower-like FeS/Fe<sub>2</sub>O<sub>3</sub> composite for lithium storage, *J. Power Sources* 392 (2018) 193–199.
- [36] M. Sun, X. Sheng, S. Li, Z. Cui, T. Li, Q. Zhang, F. Xie, Y. Wang, Construction of porous CoTiO<sub>3</sub> microrods with enhanced performance as lithium-ion battery anode, *J. Alloys Compd.* 926 (2022) 166809.